

Interplay between Elastic and Electrochemical Properties during Active Material Transitions and Aging of a Lithium-Ion Battery

Simon Feiler⁺^[a], Philip Daubinger⁺^[a], Lukas Gold,^[a] Sarah Hartmann,^[a] and Guinevere A. Giffin^{*[a, b]}

The interplay between the internal mechanical properties and external mechanical conditions of a battery cell, e.g., Young's modulus and thickness change, has a crucial impact on the cell performance and lifetime, and thus, needs to be fully understood. In this work, 12 Ah lithium-ion battery pouch cells were studied during cycling and aging by non-invasive operando ultrasonic and dilation measurements. The effective Young's modulus increases and the thickness varies the most within a

single cycle during the graphite transition from stage 1L to 4, at the beginning of the 2 to 1 stage transition and at the phase transition of the nickel-rich NCM from H2 to H3. After 1000 cycles of aging, the overall effective Young's modulus of the lithium-ion battery decreases by ~11%–12% and the cell thickness increases irreversibly by ~3%–4%, which is mostly related to a thicker and possibly softer, more porous solid electrolyte interphase layer.

Introduction

For today's lithium-ion batteries (LIBs), lifetime and reliability play an increasingly important role in the environmental impact, performance, safety and costs. In addition to the well-studied effects of current and temperature on the longevity of LIBs, another key element to consider is the mechanical and electrochemical interplay of the batteries. This interplay, between, e.g., electrode expansion,^[1–4] changes in elastic properties such as Young's modulus^[5,6] and changes in porosity^[7–9] during cycling and aging, can have a significant impact on the performance and degradation of LIBs. Along with the importance of the internal mechanical properties on the lifetime of LIBs, the external mechanical conditions, e.g., bracing, also have a significant impact. An external mechanical pressure applied on the batteries can be beneficial as it, e.g., counteracts contact losses of electrodes with the separator.^[9–12]

A method to study the mechanical changes inside a LIB during cycling that has become more popular in recent years is the use of ultrasound.^[13–15] In this method, an ultrasonic

transducer is acoustically coupled to the battery and the transmitted or the reflected signal is recorded and analyzed. Changes in thickness or stiffness of the whole cell, e.g., caused by changes in the lattice structure of the electrodes during cycling, result in changes in the measured signal. One obtainable parameter from the ultrasonic measurements is the time of flight (ToF), defined as the time it takes for the ultrasonic wave to travel through a battery. Together with the thickness d of the cell, the mean sound velocity c of the whole cell can be calculated:

$$c = \frac{d}{\text{ToF}} \quad (1)$$

The sound velocity is dependent on the effective Young's modulus E_{eff} , defined as:^[16]

$$c = \sqrt{\frac{E_{\text{eff}}}{\rho}} \quad (2)$$

where ρ is the overall density of the battery cell. The effective Young's modulus is a unit of measure for the stiffness of the cell. A lower modulus indicates a softer cell and leads to a lower sound velocity.

The term *effective modulus* was proposed by Knehr et al.^[16] to summarize the elastic interactions of the different layers into a single parameter for the cell as a whole. This effectively treats the cell as an isotropic medium which is justifiable by the fact that the ultrasonic wavelength used is much larger than the thickness of the individual layers.^[17] In this definition, the shear modulus is neglected for simplicity. It also includes emergent effects on the sound velocity that arise from the layered structure, e.g., as described in Ref. [18].

It has been shown that ultrasonic testing, and in particular the ToF, is sensitive to mechanical battery degradation. An

[a] S. Feiler,⁺ P. Daubinger,⁺ L. Gold, Dr. S. Hartmann, Dr. G. A. Giffin
Fraunhofer R&D Center Electromobility
Fraunhofer Institute for Silicate Research
Neuerplatz 2, 97082 Würzburg (Germany)
E-mail: guinevere.giffin@isc.fraunhofer.de

[b] Dr. G. A. Giffin
Julius-Maximilians-Universität Würzburg (JMU)
Faculty of Chemistry and Pharmacy
Chemical Technology of Materials Synthesis
Röntgenring 11, 97070 Würzburg (Germany)

[†] These authors contributed equally to this work.

 Supporting information for this article is available on the WWW under
<https://doi.org/10.1002/batt.202200518>

 © 2023 The Authors. *Batteries & Supercaps* published by Wiley-VCH GmbH.
This is an open access article under the terms of the Creative Commons Attribution License, which permits use, distribution and reproduction in any medium, provided the original work is properly cited.

increase in the ToF is observed during the first 300 or less cycles.^[19–22] Knehr et al.^[16] measured a rapid increase in ToF and dilation of the cell during the first 12 cycles which they attributed to the initial swelling of the graphite anode and changes in its elastic modulus. They observed that this trend continues, albeit much slower, up to 100 cycles. However, there is no long-term data available to confirm whether this trend continues during the typical lifetime of today's batteries. Bommier et al.^[23] measure a ToF increase during the first 700 cycles, however, without measuring the thickness of the cells. Thus, a conclusion cannot be drawn whether the effect is due to a thickness increase or a decrease in elastic modulus or both. In general, the survey of the published literature has shown that the relevant mechanical changes in a LIB cell are either studied for a small number of cycles or without taking the thickness change into account.

In this work, the dependence of the mechanical properties on the state-of-charge (SoC) in commercial 12 Ah LIB cells are studied with ultrasound and dilatometry. The correlation of the ultrasonic signal with the electrode transitions is examined. Furthermore, the mechanical changes are examined during an aging test with 1000 cycles. The correlation between the change in the capacity, thickness and ToF is shown.

Results and Discussion

Figure 1 shows the initial reference performance test (RPT) of the 12 Ah LIB pouch cell. During charging and discharging (at 0.04 C), the thickness of the LIB cell varies by ~0.13 mm, which corresponds to ~2.0% of the total value of ~6.5 mm (Figure 1a and b). A plateau in the thickness can be seen at ~3.7 V, which can probably be associated with the graphite anode. The graphite electrode undergoes small thickness changes during the 3L-2 stage transition that occurs around 50% SoC.^[3,4,24,25] The cathode has a thickness change that is an order of magnitude smaller in the SoC 0–80% region.^[4,25,26] At high SoCs, starting at ~4.1 V, a decline in thickness of the cell is detected. Here, the nickel-rich NCM cathode contracts, as the c-lattice parameter in the rhombohedral crystal structure of the layered oxide cathode declines.^[4,25–27] Even though the cell is expanding during charge, the ToF decreases (Figure 1c). This is initially counterintuitive as the cell is getting thicker and the signal needs to traverse a greater distance. However, it can be explained by an increase in the sound velocity (Figure 1d), which leads to the decrease in the ToF [Equation (1)]. The change in the sound velocity is dependent on the change in stiffness of the electrodes inside the cell [Equation (2)]. The anode is mostly responsible for the increased stiffness during charging,^[6] which results in an increase in the effective Young's modulus of ~9% of the whole cell (Figure 1e). The cathode also shows a change in effective Young's modulus, but this change is less pronounced when compared to the anode.^[28] During discharge, the reverse process takes place.

Overall, it can be concluded that the ultrasonic measurements detect mechanical changes inside a battery during cycling. A more detailed examination of the correlation

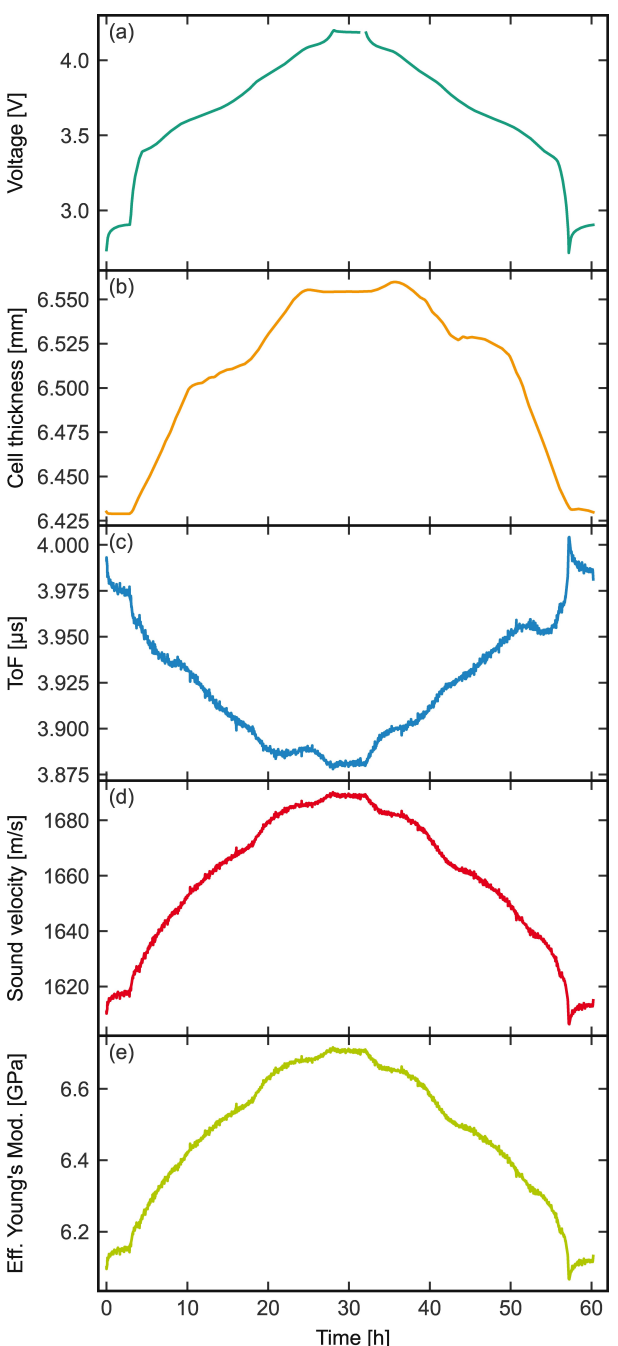


Figure 1. Parameters of an initial single cycle at 0.04 C of a 12 Ah LIB: a) voltage, b) cell thickness, c) ToF, d) sound velocity and e) effective Young's modulus as a function of time.

between the change in the capacity, thickness and ToF will be discussed later.

After the initial RPT, the cells are cycled for 1000 cycles with a C-rate of 1.0 C. After every 200 cycles, a RPT is performed (Figure 2). The cells have a relatively high-capacity retention of ~95% after 1000 cycles. The discharge capacity, when comparing the initial and final RPT, drops by ~10%, with the largest drop occurring between the initial RPT and that at cycle 200. This is probably due to incomplete wetting of the electrodes, and hence, further solid electrolyte interphase (SEI) growth,

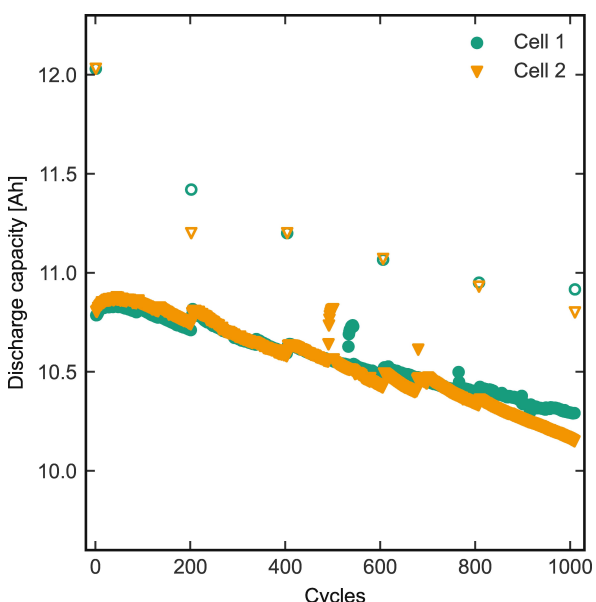


Figure 2. Discharge capacity of the 12 Ah LIB cell during aging at 1.0 C. The unfilled circles correspond to capacity measurements from the RPT at 0.04 C. Cells were aged with a bracing of 10 kPa.

most likely in the first few of the 200 cycles, which consumes cyclable lithium causing the capacity to fade. The capacity increases during the first ca. 60 cycles at 1.0 C, which may be related to the cracking of the active materials leading to shorter diffusion pathways within the particles. Therefore, at this high C-rate, more active material takes part in the electrochemical reaction leading to an increase in capacity.

To further examine the SEI formation and the capacity reduction during the aging test, electrochemical impedance spectroscopy (EIS) was performed during the RPT cycles at SoC 50% (Figures 3 and S1). The data was fitted with the equivalent circuit model shown in Figure S2. Figure 3 shows that the decrease of the resistance after the initial RPT is mostly caused by the drop of the SEI resistance (R_{SEI}). It should be noted that R_{SEI} includes the resistance of the surface layers on the anode and cathode, although the contribution of anode SEI layer is dominant. The decline in the R_{SEI} after the initial RPT may seem counterintuitive, particularly in association with the SEI growth as described above. However, the particle cracking and filling of pores not yet wetted with electrolyte leads to an increase in the electrochemically active surface area. The exposure of more surface area reduces the resistance and increases the capacity in the initial ~60 cycles at 1.0 C (Figure 2). Figure 3b shows that after cycle 200, the R_{SEI} starts to increase slightly due to thickening of the SEI. This effect probably started earlier but was concealed by the exposure of fresh active material surface area. The trends in the impedance data further substantiate the explanation of incomplete wetting during formation.^[16] The ohmic resistance (R_S) increases constantly from ~2.0 mΩ to ~2.3 mΩ during aging. The charge transfer resistance (R_{ct}) is more or less constant at ~0.9 mΩ in the first 400 cycles, followed by an increase up to ~1.4 mΩ at cycle 1000.

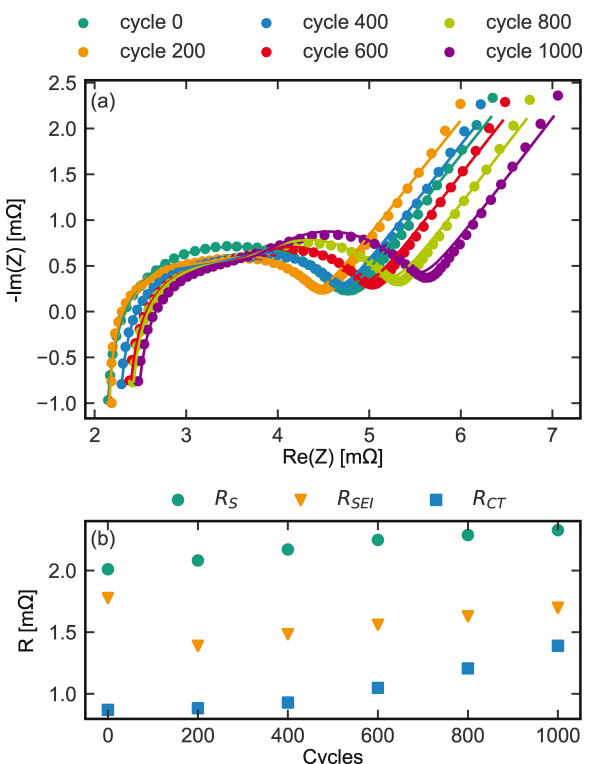


Figure 3. Evolution of the EIS measurement parameters during cycling of Cell 1: a) Nyquist plot and b) ohmic (R_S), SEI (R_{SEI}) and charge transfer resistance (R_{ct}) over the cycles.

After evaluating the capacity reduction and the impedance growth during aging, a closer examination of the changes of the mechanical parameters during the RPTs is performed. Figure 4a shows the differential voltage analysis, while the incremental capacity analysis for the RPTs during the aging study is seen in Figures S3 and S4. For peak identification, electrode material was harvested from a fresh cell and laboratory full cells with a lithium reference electrode were built. The results can be seen in Figures S5 and S6. The first peak (I, Figure 4a) can mainly be attributed to the transition of graphite stages 1L-4. The next two peaks are both a superposition of a cathode phase transition and a graphite stage transition, i.e., H1-M with 3-2 (II) and M-H2 with 2-1 (III), respectively. The last one (IV) can be solely attributed to the H2-H3 phase transition.^[29] As the most mechanical changes are expected from the anode, the graphite stage transitions are overlaid in different colors in Figure 4 to serve as an orientation. Cycle 0 shows a large deviation in dQ/dV from the other cycles. This is likely due to break-in effects where the electrolyte further infiltrates the porous electrodes. The capacity increase during the initial cycles and the decrease in SEI resistance support this claim. Afterwards, the changes are less drastic (Figures 2, 3 and 4a). During RPT of cycles 200 through 1000, the first three peaks in the dQ/dV plot shift to higher voltages (a delta of ~20 mV in total) and decrease in height as the cell ages (Figure 4a). This can be attributed to the loss of cyclable lithium, which is associated with SEI growth, and is evident in an increase in SEI resistance. Less cyclable

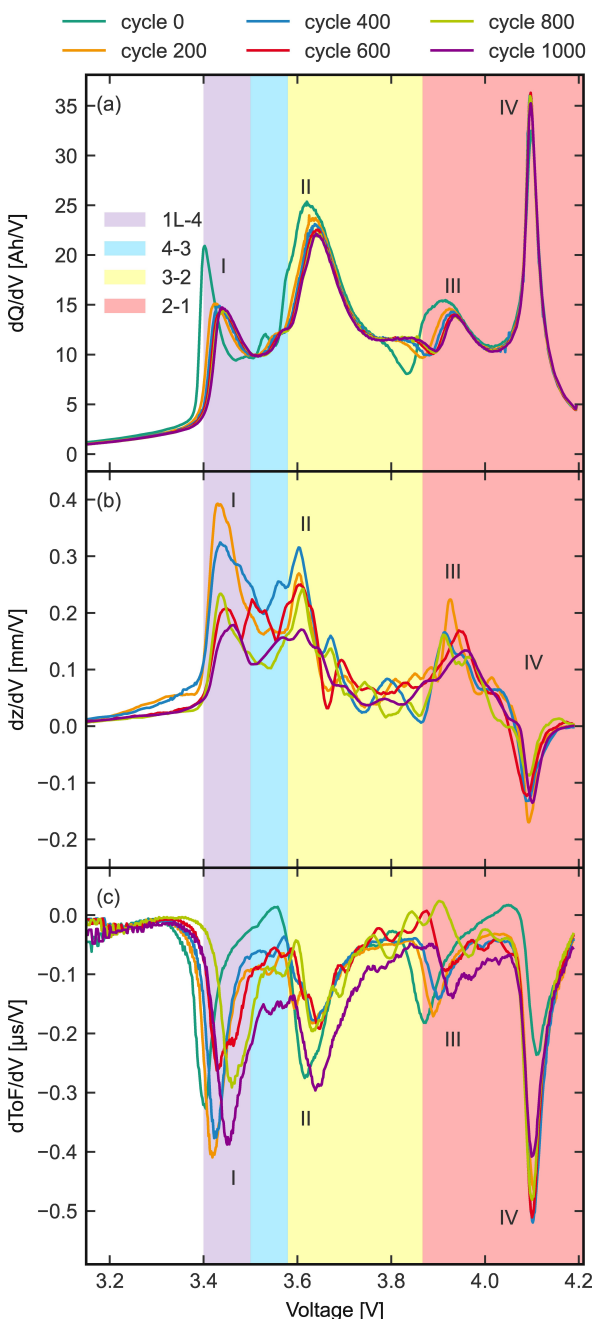


Figure 4. Differential analysis of a) capacity, b) dilation and c) ToF for 0.04 cycles during RPT over cell voltage of Cell 1. The colored overlay shows the staging of the graphite estimated from three electrode laboratory cells (Figures S5 and S6).

lithium leads to a less lithiated anode at a given voltage, therefore shifting the intercalation stages of graphite to higher cell voltages. The last peak is not affected as it can purely be attributed to the NCM.^[29]

Figure 4b shows the incremental dilation analysis of the RPT cycles 200–1000. For cycle 0, there was no data recorded. When comparing the increase in thickness with the stages of graphite, it can be observed that a major contribution of the cell expansion stems from the graphite stages 1L through 3. For the 3-2 stage transition, the change in thickness decreases.

The 2-1 transition also leads to a major increase in thickness but is counteracted by the decrease in thickness of the H2-H3 phase transition of the nickel-rich NCM. This explains the upward trend at around 3.9 V (III) followed by the decrease in differential thickness at around 4.1 V (IV). This can also be seen in the overall thickness change (Figure 1b). During the aging of the cell, the clearest trend is the decrease of reversible thickness gain during the 1 L-3 transition, i.e., between ~3.4–3.5 V. This could be due to particle cracking on the cathode and/or SEI formation on the anode. Both processes can lead to higher porosity that can accommodate part of the expansion. It should be noted that the oscillations of the signals stem from stick and slip effects of the profile rail guides from the bracing setup.

Figure 4c shows the differential ToF over voltage. Four peaks can be observed, (I–IV) in Figure 4c. The second peak (II) mainly stems from a voltage plateau, that mathematically leads to a larger absolute $d\text{ToF}/dV$, rather than a significant change in ToF. This is confirmed by the absence of this peak in the $d\text{ToF}/dQ$ plots in Figure S3c. A negative differential ToF (ToF is decreasing) can be caused by a decrease in thickness ($-dz/dV$) and/or by an increase in stiffness and therefore an increase in sound velocity. A peak in the differential ToF means that the changes in stiffness and/or thickness are confined or enhanced in a specific region, in our case a specific voltage range. In a battery, changes in the lattice structure of the electrodes, e.g., stage or phase transitions due to lithium intercalation, are therefore expected to cause peaks in the ToF.

The first peak (I) stems from the 1L-4 transition of graphite. The peak is caused by a stiffening of the graphite anode. The reason cannot be a decrease in thickness because the anode is expanding (Figure 4b) in that stage. The same logic applies to the third peak (III) that occurs right after the completion of stage 2. The shifting and position of the peak suggest that this is an effect of the anode, although a contribution of the M–H2 phase transition of the NCM cathode cannot be ruled out. With the completion of stage 2, lithium-ions start to intercalate between every graphene layer. Therefore, the mechanical properties, e.g., the Young's modulus (thus, ToF) and the thickness of the graphite electrode change drastically at this point. The peak does not span over the whole 2-1 transition but is located at the start of the stage transition. This indicates that the major part of the mechanical changes during this transition are taking place in the initial lithium-ion intercalation of the 2-1 stage transition. The last peak (IV) stems mainly from the cathodic H2-H3 phase transition. Here, it must be distinguished whether the peak is an effect of the decreased thickness or of the increase in stiffness. Assuming a constant sound velocity of 1680 m/s, the differential dilation of $\sim -0.15 \text{ mm/V}$ would only lead to a differential ToF of $-0.1 \mu\text{s/V}$ for the last peak, but a change of $\sim -0.5 \mu\text{s/V}$ is measured. Thus, this change in ToF is mostly caused by an increase in effective Young's modulus during this H2-H3 transition and not due to a decline in cell thickness. During aging, the peaks of the graphite anode (I and III) shift to higher voltages and decrease in magnitude due to loss of cyclable lithium. The peak of the H2-H3 transition does not change notably. It should be

noted that in cycle 1000, the ultrasonic measurement was conducted at a different spot on the cell, due to coupling problems. An inhomogeneous thickness increase of the cell led to an insufficient coupling of the ultrasonic wave into the battery cell on the previous measuring spot. The result is that the data is not fully comparable to the prior RPTs.

The absolute ToF is shown in Figures 5(a) and S7 for the RPT cycles. It can be seen that the ToF increases from cycle 0 to cycle 1000. During aging, the cell undergoes an irreversible thickness growth from ~6.5 mm before cycling to ~6.75 mm at cycle 1000. This results in a longer sound path for the ultrasonic signal through the battery that would account for ~0.15 μ s of travelling time, assuming an unchanged sound velocity from cycle 0. Nevertheless, the total increase in ToF is ~0.4 μ s. Thus, the additional increase must be related to a reduction of the overall stiffness of the cell, which can be seen in Figure 5b. The effective Young's modulus decreases by 0.7 GPa–0.8 GPa, which corresponds to 11%–12%. The reversible modulus change between charged (SoC 100%) and discharged state (SoC 0%) also decreases from around 0.58 GPa to 0.43 GPa, when comparing the initial cycle to cycle 1000. This reveals that the cell is not only getting thicker but also softer during aging. The decrease in Young's modulus can be related to a possibly softer and more porous SEI over aging.^[30–32] A higher porosity leads to a lower sound velocity in the medium. This mechanism is well known in geophysics.^[33,34] Larger pores deform more easily under stress, implying that they are softer and thus, lower the

sound velocity. It should be noted that the values of cycle 0 is from a different unaged reference cell, because logging of the dilation, which is needed for determining the effective Young's modulus [Equations (1) and (2)] was introduced at cycle 200.

Conclusion

Ultrasonic and dilation measurements on commercial 12 Ah LIB pouch cells reveal mechanical changes inside the cell. During a single cycle, an increase in the effective Young's modulus of ~9% from fully discharged (SOC 0%) to fully charged state (SOC 100%) is measured. This change probably stems in large part from the graphite anode and the H₂-H₃ phase transition of the NCM. Most of the ToF decrease and hence stiffening of the cell is observed during the graphite transition 1L-4, at the beginning of 2-1 transition and at the phase transition of the nickel rich NCM from H₂-H₃. The largest increase in thickness during a cycle of the cell is observed during the graphite transitions 1L-3 and at the beginning of 2-1 followed by a decrease in thickness from the H₂-H₃ transition.

During aging, the reversible change in thickness decreases, while the irreversible thickness of the cell increases, probably mostly due to SEI formation and cracking. This leads to a higher porosity of the cell that can partially accommodate the expansion of the electrodes during cycling. The magnitude of the differential ToF during cycling is decreasing, mostly in SoC regions where the anode has stage transitions. The differential ToF during the cathodic H₂-H₃ transition does not experience significant changes during aging. From cycle 0 to 1000 a decrease in the cells effective Young's modulus of 11%–12% is measured. This softening can probably mostly be attributed to the graphite anode. The irreversible thickness increase combined with an increase in SEI resistance is an indication of a growing SEI layer on the anode. The SEI is possibly softer and more porous than the rest of the cell, which lowers the overall cell modulus and increases ToF. A schematic of the findings of this work are shown in Figure 6. The methodology demonstrated presents a chance for a fundamentally different perspective towards battery diagnostics by studying mechanical parameters instead of electrical ones which might be more sensitive and/or easier to implement in certain conditions. Analyzing the time of flight has been shown to reliably correlate with capacity fading of the cell and staging of the graphite anode over 1000 cycles.

Experimental Section

Electrochemical testing: For all experiments, two LIBs with a nominal capacity of 12 Ah from Kokam (SLPB065070180, Kokam Co., Ltd.) were used. The cell consists of a graphite anode and a nickel-rich NCM cathode. It is known from the data sheet that the electrolyte is a mixture of lithium hexafluorophosphate (LiPF₆) in ethylene carbonate (EC)/ethyl methyl carbonate (EMC), but the exact composition is not given. The battery cells have an active area dimension (excluding sealing and tabs) of 67 mm × 165 mm (width × height). The thickness of the battery cell is 6.5 mm ±

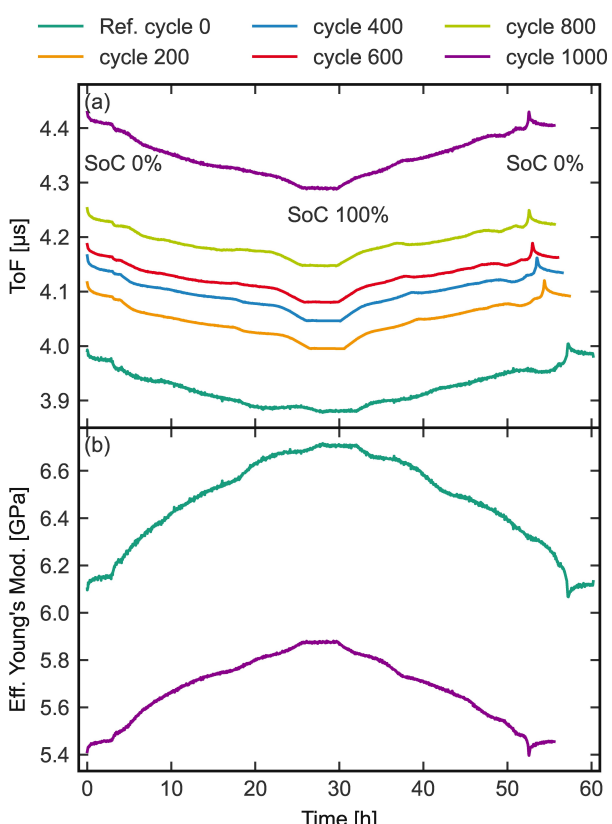


Figure 5. a) Evolution of ToF and b) effective Young's modulus as a function of time during RPTs of Cell 1.

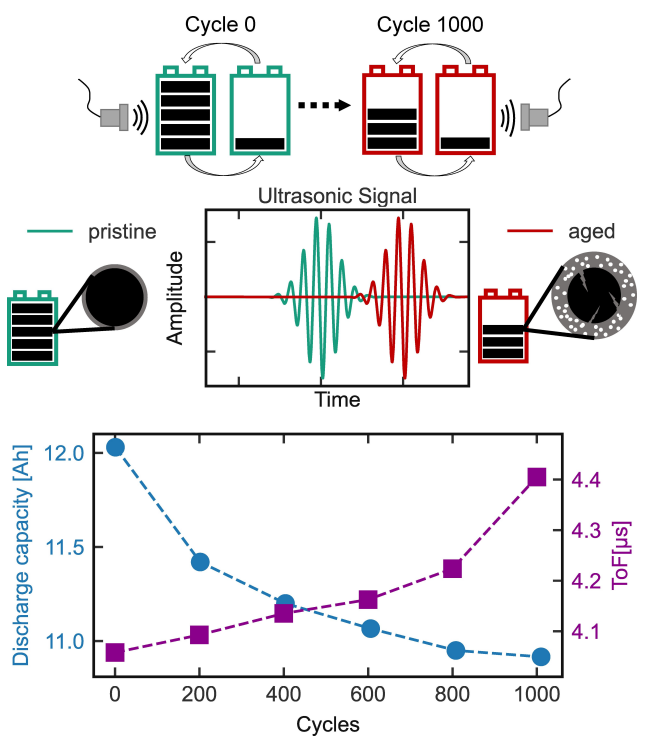


Figure 6. Schematic of the findings of this work, which illustrates the generalization of morphological changes on the particle level.

0.05 mm at SoC 30%. The RPT was performed in self-built experimental setup (Figure 7). The applied external pressure was 10 kPa and the cycling was performed within the voltage range of 2.7 V to 4.2 V. The C-rate during constant current constant voltage

(CCCV) charging and CC discharging in the RPT (measured with a Biologic SP-240, BioLogic Sciences Instruments) was 0.04 C (0.48 A). The cut-off criterion in the constant voltage step during charge was a current $I < 0.01$ C at 4.2 V. After reaching the charging cutoff criterion, a 3 h rest period was included. During the accelerated aging tests, the cells were braced in a separate spring braced device at a pressure of 10 kPa and cycled from 2.7 V to 4.2 V at a rate of 1.0 C (12.0 A) also using a CCCV charge and CC discharge procedure (Maccor Series 4000, Maccor Inc.). The cut-off criterion during charging in the voltage step was a current $I < 0.1$ C at 4.2 V. After charging and discharging, a 10 minute rest step was included.

Experimental setup: A sketch of the test setup is shown in Figure 7. The pressure was applied through two springs (38.15 N/mm, 13330, SODEMANN Industriefjedre A/S) to ensure a control of the pressure by ± 1 kPa. The cells were braced between two 25 mm thick aluminum plates in order to apply a homogeneous pressure distribution. A pressure sensor (KM38-2 kN load cell, ME-Systeme GmbH) was used to measure the force applied on the battery cell. The expansion of the battery cell was measured with a dilation sensor (IL-S065, KEYENCE DEUTSCHLAND GmbH) paired with an amplifier unit (IL-1000, KEYENCE DEUTSCHLAND GmbH). The ultrasonic transducers (U2P10, United NDT GmbH) had a center frequency of 2.0 MHz and a diameter of 10 mm. The transducers were mounted flat on the backside of each metal plate, facing each other. To enhance the coupling, and thus reduce reflections at the different interfaces (transducer-metal plate, metal plate-battery), canola oil was used as a coupling agent.

Ultrasonic measurements: For all excitation pulses and recordings, a single-channel ultrasonic frontend (PCUS pro Single, Fraunhofer Institute for Ceramic Technologies and Systems IKTS) was used. The excitation voltage of the applied rectangular pulse was set to 200 V with a pulse length of 500 ns. The excited ultrasonic signal passes through the metal plates and the LIB and was recorded by

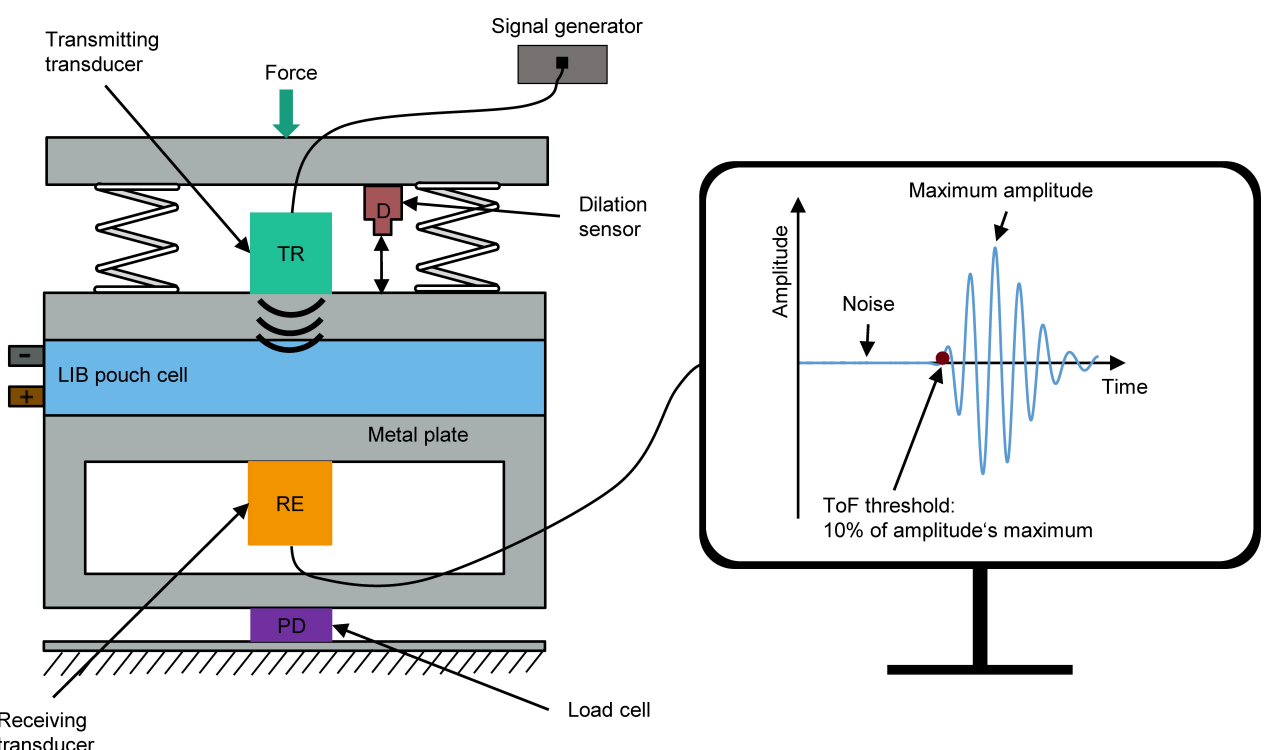


Figure 7. Scheme of experimental setup and an exemplary incoming ultrasonic signal.

the PCUS analog digital converter with a sampling rate of 100 MHz. On the right hand side of Figure 7, an exemplary ultrasonic signal is shown. To evaluate the ToF, a thresholding method was used (Figure 7). The ToF is taken as the first datapoint of the entry exceeding the threshold. The threshold was set to 10% of the maximum amplitude. The value was chosen as a good compromise between detecting the signal as early as possible and staying well above the noise level. Scaling the threshold with the maximum amplitude ensures that the ToF is independent of the scale of the signal as the intersection of the threshold with the signal is located at the same point in time for two differently scaled signals. The signals are prefiltered by a hardware filter with center frequency at 2 MHz and detrended by subtracting a linear least-squares fit from the data. To enhance the resolution of the ToF beyond the 10 ns (limited by the 100 MHz sampling rate) of the A/D converter, the signal was linearly interpolated between the first datapoint exceeding the threshold and the previous datapoint. The ToF of the LIB is determined by a subtraction of the ToFs through the setup with and without the LIB.

Electrochemical impedance spectroscopy

EIS measurements were conducted for SoC 0%, 50% and 100%. SoC 0% is defined as the recommended discharge cut-off voltage at 2.7 V. SoC 100% is the charge cut-off voltage at 4.2 V. SoC 50% is defined as the state of the cell at 3.7 V, which was determined from the open circuit potential of a fresh cell charged to half of the initial discharge capacity. To reach a given SoC, the cells were brought to the cutoff voltage with a 0.04 C (0.48 A) constant current, constant voltage step with an CV cutoff of $I < 0.01$ C. Impedance data was acquired with a potentiostatic EIS measurement with an amplitude of 5 mV (Biologic SP-240, BioLogic Sciences Instruments). Frequencies were recorded between 7 MHz and 10 mHz. The measurements were averaged for a given frequency and 11 points were measured per frequency decade. Data points below $\text{Im}(Z) < 1 \text{ m}\Omega$ were neglected due to occurrence of skin effect at high frequencies. A simplified equivalent circuit, represented by Equation 3 and shown in Figures S2, e.g., as used in Ref. [34], was used to fit the data. The real and imaginary impedance data were raveled/flattened and a least square fit was conducted. The capacitances were approximated as constant phase elements and the Warburg element Y_0 was extended by an additional angle parameter γ .

$$Z = i\omega L + R_S + \frac{1}{\frac{1}{R_{SEI}} + (i\omega)^\beta C_{SEI}} + \frac{1}{\frac{1}{R_{CT} + \frac{1}{Y_0 \sqrt{\omega} e^{j\gamma}}} + (i\omega)^\alpha C_{CT}} \quad (3)$$

Author Contributions

S. F. and P. D. contributed equally to this work. Conceptualization, Investigation, Methodology, Visualization and Writing – original draft was done by S. F and P. D. Investigation, Supervision and Writing – review & editing was performed by L. G, S. H and G. G.

Acknowledgements

The authors gratefully acknowledge the funding of this work by the European Union's Horizon 2020 Research & Innovation program in the SPARTACUS project (grant number 957221) and

the Federal Ministry of Education and Research (BMBF) of Germany in the project MAD³AM4Life (grant number 03XP0327). We also want to thank the members of the Fraunhofer R&D Center Electromobility and the Center Smart Materials and Adaptive Systems at Fraunhofer ISC for fruitful discussions and scientific support. Open Access funding enabled and organized by Projekt DEAL.

Conflict of Interest

The authors declare no conflict of interest.

Data Availability Statement

The data that support the findings of this study are available from the corresponding author upon reasonable request.

Keywords: aging · lithium · phase transition · ultrasound · Young's modulus

- [1] D. Sauerteig, S. Ivanov, H. Reinhagen, A. Bund, *J. Power Sources* **2017**, 342, 939.
- [2] B. Rieger, S. Schlueter, S. V. Erhard, J. Schmalz, G. Reinhart, A. Jossen, *J. Energy Storage* **2016**, 6, 213.
- [3] P. Daubinger, F. Ebert, S. Hartmann, G. A. Giffin, *J. Power Sources* **2021**, 488, 229457.
- [4] F. B. Spangler, S. Kücher, R. Phillips, E. Moyassari, A. Jossen, *J. Electrochem. Soc.* **2021**, 168, 40515.
- [5] K. Min, E. Cho, *Phys. Chem. Chem. Phys.* **2018**, 20, 9045.
- [6] Y. Qi, H. Guo, L. G. Hector, A. Timmons, *J. Electrochem. Soc.* **2010**, 157, A558.
- [7] S. A. Channagiri, S. C. Nagpure, S. S. Babu, G. J. Noble, R. T. Hart, *J. Power Sources* **2013**, 243, 750.
- [8] G. Sikha, B. N. Popov, R. E. White, *J. Electrochem. Soc.* **2004**, 151, A1104.
- [9] M. Göttlinger, P. Daubinger, W. Stracke, S. Hartmann, G. A. Giffin, *Electrochim. Acta* **2022**, 419, 140354.
- [10] P. Daubinger, M. Schelter, R. Petersohn, F. Nagler, S. Hartmann, M. Herrmann, G. A. Giffin, *Adv. Energy Mater.* **2022**, 12, 2102448.
- [11] J. Cannarella, C. B. Arnold, *J. Power Sources* **2014**, 245, 745.
- [12] M. Wünsch, J. Kaufman, D. U. Sauer, *J. Energy Storage* **2019**, 21, 149.
- [13] L. Gold, T. Bach, W. Virsik, A. Schmitt, J. Müller, T. E. M. Staab, G. Sextl, *J. Power Sources* **2017**, 343, 536.
- [14] A. G. Hsieh, S. Bhadra, B. J. Hertzberg, P. J. Gjeltema, A. Goy, J. W. Fleischer, D. A. Steingart, *Energy Environ. Sci.* **2015**, 8, 1569.
- [15] R. J. Copley, D. Cumming, Y. Wu, R. S. Dwyer-Joyce, *J. Energy Storage* **2021**, 36, 102406.
- [16] K. W. Knehr, T. Hodson, C. Bommier, G. Davies, A. Kim, D. A. Steingart, *Joule* **2018**, 2, 1146.
- [17] J. M. Carcione, *J. Acoust. Soc. Am.* **1996**, 99, 2655.
- [18] G. E. Backus, *J. Geophys. Res.* **1962**, 67, 4427.
- [19] J.-Y. Kim, J.-H. Jo, J.-W. Byeon, *Microelectron. Reliab.* **2020**, 114, 113859.
- [20] P. Ladpli, F. Kopsaftopoulos, F.-K. Chang, *J. Power Sources* **2018**, 384, 342.
- [21] Y. Wu, Y. Wang, W. K. C. Yung, M. Pecht, *Electronics* **2019**, 8, 751.
- [22] G. Davies, K. W. Knehr, B. van Tassell, T. Hodson, S. Biswas, A. G. Hsieh, D. A. Steingart, *J. Electrochem. Soc.* **2017**, 164, A2746–A2755.
- [23] C. Bommier, W. Chang, J. Li, S. Biswas, G. Davies, J. Nanda, D. I. Steingart, *J. Electrochem. Soc.* **2020**, 167, 20517.
- [24] M. Bauer, M. Wachtler, H. Stöwe, J. V. Persson, M. A. Danzer, *J. Power Sources* **2016**, 317, 93.
- [25] H. Pegel, O. von Kessel, P. Heugel, T. Deich, J. Tübke, K. P. Birke, D. U. Sauer, *J. Power Sources* **2022**, 537, 231443.
- [26] L. de Biasi, A. O. Kondrakov, H. Geßlein, T. Brezesinski, P. Hartmann, J. Janek, *J. Phys. Chem. C* **2017**, 121, 26163.

- [27] P. Kargl, V. Drews, P. Daubinger, O. Schweighofer, M. Marinaro, G. A. Giffin, M. Wohlfahrt-Mehrens, A. Thaler, *J. Power Sources* **2022**, *548*, 232042.
- [28] R. Xu, H. Sun, L. S. de Vasconcelos, K. Zhao, *J. Electrochem. Soc.* **2017**, *164*, A3333–A3341.
- [29] R. Jung, M. Metzger, F. Maglia, C. Stinner, H. A. Gasteiger, *J. Electrochem. Soc.* **2017**, *164*, A1361–A1377.
- [30] P. Guan, L. Liu, X. Lin, *J. Electrochem. Soc.* **2015**, *162*, A1798–A1808.
- [31] S. K. Heiskanen, J. Kim, B. L. Lucht, *Joule* **2019**, *3*, 2322.
- [32] W. Huang, P. M. Attia, H. Wang, S. E. Renfrew, N. Jin, S. Das, Z. Zhang, D. T. Boyle, Y. Li, M. Z. Bazant, B. D. McCloskey, W. C. Chueh, Y. Cui, *Nano Lett.* **2019**, *19*, 5140.
- [33] C. M. Sayers, L. D. den Boer, *Geophys. Prospect.* **2021**, *69*, 1733.
- [34] M. R. J. Wyllie, A. R. Gregory, L. W. Gardner, *Geophys.* **1956**, *21*, 41.

Manuscript received: December 1, 2022
Revised manuscript received: January 25, 2023
Version of record online: February 13, 2023
